

PAPER • OPEN ACCESS

A biomimetic chiral auxetic vertebral meta-shell

To cite this article: A Sorrentino *et al* 2024 *Smart Mater. Struct.* **33** 105044

View the [article online](#) for updates and enhancements.

You may also like

- [Fluid dynamic parameters of naturally derived hydroxyapatite scaffolds for *in vitro* studies of bone cells](#)
E Salerno, A d'Adamo, G Corda et al.
- [Vision-based dynamic monitoring of a steel footbridge](#)
E. Buoli, E. Bassoli, G. Eslami Varzaneh et al.
- [A proposal of VnR-based dynamic modelling activities to introduce students to model-centred learning](#)
Federico Corni and Enrico Giliberti



ECS The Electrochemical Society
Advancing solid state & electrochemical science & technology



ECS UNITED

247th ECS Meeting
Montréal, Canada
May 18-22, 2025
Palais des Congrès de Montréal

Showcase your science!

Abstracts due December 6th

A biomimetic chiral auxetic vertebral meta-shell

A Sorrentino^{1,*} , K Genovese², L Nicolini¹ and D Castagnetti¹ 

¹ Dipartimento di Scienze e Metodi dell'Ingegneria, Università di Modena e Reggio Emilia, Via G. Amendola 2, 42122 Reggio Emilia, Italy

² Scuola di Ingegneria, Università degli Studi della Basilicata, Viale dell'Ateneo Lucano 10, 85100 Potenza, Italy

E-mail: andrea.sorrentino@unimore.it, katia.genovese@unibas.it, lorenzo.nicolini@unimore.it and davide.castagnetti@unimore.it

Received 15 May 2024, revised 13 August 2024

Accepted for publication 18 September 2024

Published 30 September 2024



CrossMark

Abstract

The work presents a novel thin-walled biomimetic auxetic meta-shell for patient-specific vertebral orthopedic implants. The proposed design stemmed from the concept of an intrinsically multiple curved auxetic meta-structure, which is created by folding a two-dimensional bio-inspired chiral geometry according to the morphology of human vertebral cortical bones. Through a multi-view stereo digital image correlation system, we investigated the mechanical response of a bio-grade titanium (Ti6Al4V ELI) additively manufactured prototype of the meta-structure under compressive loadings. In addition, we analyzed the morphology of the prototype using a scanning electron microscopy and an optical image dimension measurement system both before and after compressive tests. An accurate Finite Element model, which exactly reproduced the geometry of the three-dimensional printed meta-shell, was implemented and calibrated against experimental results, obtaining a precise prediction tool of its mechanical response. The findings of this work demonstrate that the designed meta-shell shows a peculiar auxetic behavior, a targeted stiffness matching to that of human vertebral bone tissues and a higher global elastic strain capability compared to those of monolithic traditional vertebral body replacements.

Supplementary material for this article is available [online](#)

Keywords: auxetic meta-biomaterials, vertebral bones, vertebral implants, stereo digital image correlation, additive manufacturing

1. Introduction

This work presents a biomimetic chiral auxetic meta-shell as a bone-mimicking vertebral meta-biomaterial for 3D-printed orthopedic implants. The treatment of primary malignant and benign aggressive spinal tumors requires the reconstruction of

the segmental defect after an en-bloc resection of the vertebral body, namely vertebral body replacement (VBR), with the aim of restoring spinal length and providing adequate stability, alignment, and load-bearing capacity [1–3]. Various orthopedic implants and techniques have been described in the literature, including bone grafts [4], mesh and carbon fiber cages [5, 6], expandable implants [7], and custom-made vertebral cages realized *via* additive manufacturing (AM) [8].

Additively manufactured VBR, namely vertebral cages, represent a valid solution in VBR surgery due to the unprecedented design possibilities offered by 3D printing, allowing the fabrication of bone-mimicking vertebral implants with customized topologies and mechanical response [9]. Generally, this type of prosthetics consists of an inner porous cellular

* Author to whom any correspondence should be addressed.



Original content from this work may be used under the terms of the [Creative Commons Attribution 4.0 licence](#). Any further distribution of this work must maintain attribution to the author(s) and the title of the work, journal citation and DOI.

lattice that mimics spongy bone, and an outer thin-walled rigid shell that mimics the morphological characteristics of cortical bone, according to the original macro-structure of human vertebrae [10].

Most of the AM-ed vertebral implants reported in the literature [8, 11, 12] are fabricated from synthetic biomaterials, which feature mechanical and biological properties similar to those of native bone tissue: powder-like materials including bio-grade titanium alloys, cobalt–chromium alloy and stainless steel are typical examples [13, 14]. In particular, as artificial biomaterials interact with biological tissues, they need to provide proper osteointegration and vascularization capabilities, limiting stress shielding phenomena while avoiding the subsidence of the implant [15, 16]. Thanks to the form-freedom offered by AM, functionalized biological materials with complex micro-scale structural geometries have been proposed [17, 18]: these structures aim to achieve bone tissue regeneration capabilities and tailored mechanical properties (i.e. stiffness and relative density) [19–21]. Despite the extent of related work in the field of biomaterials, the bone regeneration and the mechanical performance of biological materials, specifically stiffness and osteointegration, are difficult to reproduce [22]. For example, a critical issue in vertebral bone reconstruction is the high stiffness of current orthopedic implants which limits the bone stimulation and the bone ingrowth around the implant, thus potentially leading to stress-shielding phenomena and ultimately prosthesis loosening [23, 24].

In this context, auxetic meta-biomaterials have attracted enormous interest worldwide due to the possibility of achieving unusual and *versatile* mechanical properties, i.e. a negative Poisson's ratio (NPR) [25, 26]. They represent a special class of bio-functionalized architected metamaterials in which the elastic (*apparent*) properties of the structure can be tailored by the rational design of its micro-architecture [27–29]. Due to their peculiar geometry, auxetic meta-biomaterials exhibit enhanced mechanical properties such as high level of energy absorption and fracture toughness [30–32]. Auxetic designs have been classified according to their unit cell geometry, which include re-entrant honeycombs, rotating units, chiral architectures, foams and folding structures [33–36], as well tubular-like designs [37–39]. However, while the mechanical behavior of re-entrant structures has been extensively studied [27, 40], limited experimental data are available on bio-auxetic designs based on chiral honeycombs and rotating units [25, 41–44], and in particular only a few works are supported by full-field strain measurements using digital image correlation techniques (DIC) [40, 45]. In addition, the mechanobiological effects of auxetic structures for bone substitution in the orthopedic implants, such as fatigue performance and bony fusion, need to be proved [46].

This work presents a novel thin-walled biomimetic auxetic meta-shell with bone-mimicking mechanical properties aimed at the development of custom-made vertebral cages for the spinal reconstruction. The proposed meta-shell was designed by folding a planar bio-inspired chiral auxetic

meta-biomaterial into an intrinsically multiple curved structure that reproduces the typical morphological profile of human vertebral cortical bones. Our idea is to design a tailored and deformable meta-shell as the basis of an innovative bio-inspired vertebral meta-implant, i.e. an orthopedic implant using meta-biomaterials, with a stiffness matching to that of human vertebrae. In particular, taking advantage of the unusual mechanical properties offered by auxetic metamaterials, the meta-shell was designed to achieve lower stiffness and higher elastic strain limit than current AM-ed vertebral cages, thus reducing implant failure and bone resorption (according to Wolff's law [47]), whilst promoting bone ingrowth. In addition, as the dimensions of the proposed meta-structure can be specifically designed according to patient features, it ensures correct stabilization of the resected portion of the spine, thus minimizing the misalignment of the vertebral column.

In order to evaluate the deformation behavior of the proposed meta-structure, an AM-ed titanium alloy prototype was fabricated and tested under a *quasi-static* compressive loading. During the experimental test, a multi-view stereo DIC system was used to measure the full-field displacement and strain maps of the meta-shell over the entire 360-deg surface. The morphology of the AM-ed meta-shell was analyzed using a scanning electron microscope (SEM) and its geometric accuracy was checked using an optical image dimension measurement system. Finally, a finite element (FE) model was implemented and validated against the experimental tests. The results showed that the proposed auxetic meta-shell exhibits a pronounced NPR, reduces the stiffness mismatch between the meta-shell and the surrounding healthy bones, and can withstand compressive loads without any significant plastic deformation up to a 3% global strain of the structure. Among other advantages, the proposed auxetic meta-shell may represent a valid solution for the design of novel porous vertebral meta-implants, whose peculiar micro-architectural feature results in a unique combination of macro-scale mechanical properties and morphology.

2. Materials and methods

2.1. Auxetic meta-shell: design and AM

This work presents a novel biomimetic vertebral auxetic meta-shell with an intrinsically multiple curvature geometry. The purpose was to design a thin-walled vertebral meta-biomaterial with bone-mimicking mechanical properties similar to those of human vertebrae, which can be adopted for the realization of custom-made additively manufactured bone replacement implants.

The elementary unit of the proposed meta-shell is based on the two-dimensional (2D) bio-inspired auxetic geometry shown in figure 1(a) [48]. This planar designed material consists of rotating chiral nodes which are interconnected by ligaments based on variable-spline curvature [49, 50], and exhibits a Poisson's ratio (PR) nearly equal to -1 [48]. Specifically, as widely explained in the previous work of Sorrentino *et al*

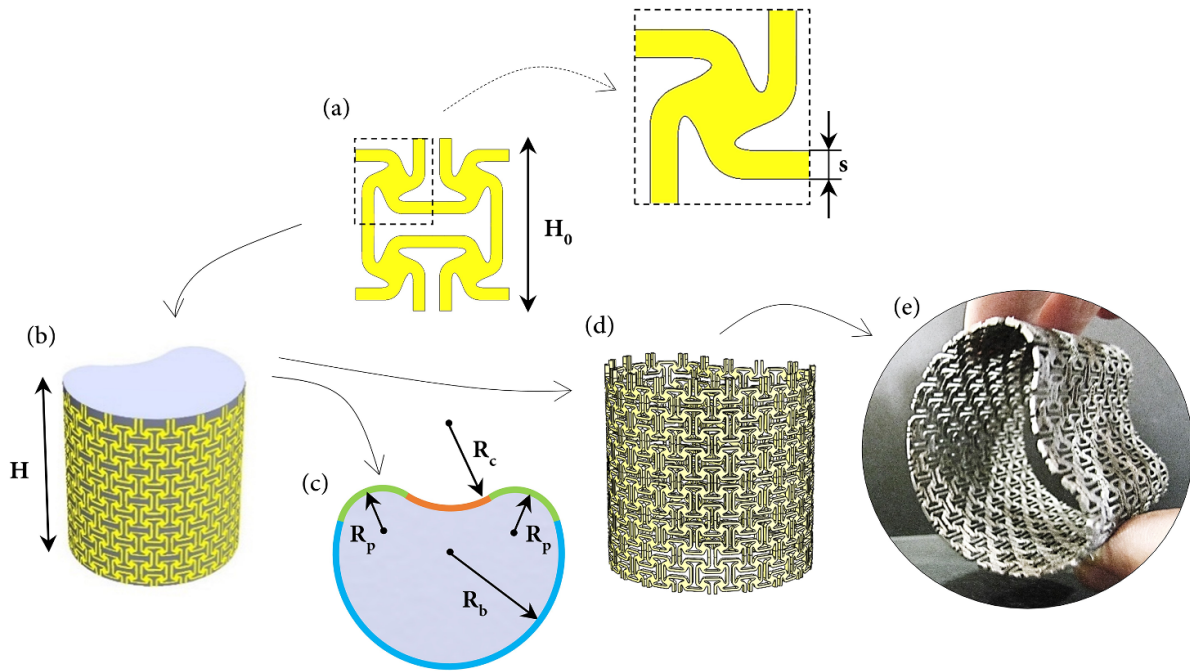


Figure 1. 2D representative unit cell with highlighted elementary unit of the meta-structure (a). Meta-shell architecture: geometric construction (b), cross-sectional view of the structure, designed meta-shell with unit thickness (d) and Ti6Al4V ELI additively manufactured prototype (e).

[48], this NPR bio-inspired design is characterized by an enhanced mass-to-strength mechanical property and a significantly higher strain capability in comparison to the classical rotating auxetic models.

Hence, to push up to the technological limits of current laser sintering techniques, and based on previous considerations on chiral architectures [48, 51], we set the thickness of the chiral ligaments s , equal to $550\ \mu\text{m}$, figure 1(a). Consequently, the length of the elementary unit of the metamaterial shown in figure 1(a), namely H_0 , is equal to 8 mm. Additional details of the structure can be found in [48].

To obtain a structure that mimics the external profile of human lumbar cortical bone, an array of the planar chiral units in figure 1(a) was folded into a 3D vertebral meta-shell (figure 1(b)). As depicted in figure 1(b), the meta-shell design consists of six unit cell layers along the longitudinal direction, resulting in a meta-shell height H of 46 mm.

Figure 1(c) shows that the metamaterial profile combines four circular sectors, tangent to each other at their intersection point, denoted as: *body* (in cyan), *peduncle* (in green) and *canal* (in orange). According to the typical shape and size of human lumbar vertebrae [52], the radii of the circular sectors R_b , R_p and R_c are approximately 22 mm, 7.5 mm and 16.5 mm, respectively. Based on the above geometric construction, figure 1(d) shows the designed vertebral meta-shell, characterized by a wall thickness equal to 1 mm.

The meta-shell design was additively manufactured from the biological-grade titanium alloy, Ti6Al4V ELI, using the selective laser melting 3D-printing process on a *M2 Dual Laser Machine* (Concept Laser), with a powder size of $25\ \mu\text{m}$, figure 1(e). Details on the chemical composition of the Ti alloy are provided in [53]. The prototype was printed along

its longitudinal direction. Moreover, due to the small size of the chiral geometry, external supports were added along the horizontal ligament of the structure. After fabrication, the prototype was finished through sandblasting, and the external supports were manually removed from the prototype. However, it is important to highlight that, to further reduce the density of the chiral meta-shell, one may replace the square-like rotating nodes in figure 1(a) with lightweight square frames without affecting the auxeticity and the elastic modulus of the structure [54]: unfortunately, this was not possible due to the directional solidification during the printing of the prototype, as well by the presence of the horizontal struts.

2.2. Morphological characterization

The prototype of the meta-shell was visually inspected both at the macroscopic level using the *Keyence IM-8030* optical image dimension measurement system, and at the microscopic level using the *Nova NanoSem 450 SE*.

On the one hand, the optical analysis revealed that the cross section of the horizontal ligaments differed slightly from the nominal shape in the CAD model. In addition, some areas of the prototype exhibited signs of warping, particularly along the peduncles and the canal sectors. Finally, the optical measurements showed that the top and bottom faces of the vertebral shell prototype were not parallel due to height inaccuracies in the vertical ligaments on both sides. Therefore, in order to implement an accurate FE model, the height of each vertical ligament was measured using the *Keyence IM-8030* system, at both the top and bottom ends of the meta-structure and reported accordingly in the numerical model.

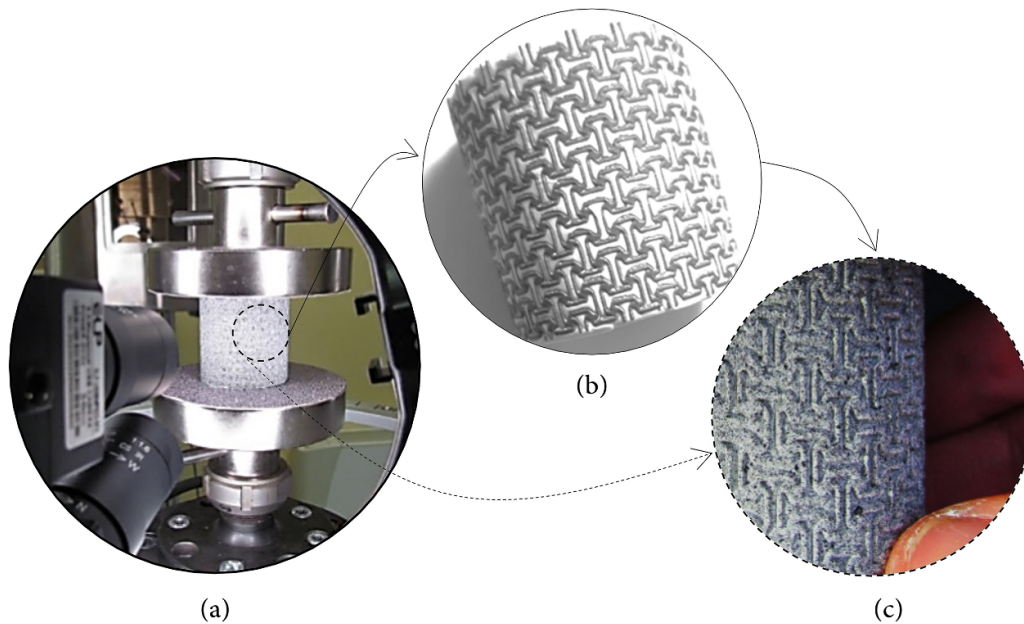


Figure 2. Picture of the experimental set-up used in the mechanical compression test (a). Preparation of the prototype for the DIC measurements: the thin layer of a soft modeling clay applied inside the meta-shell (b) and stochastic pattern on the external surface of the prototype created using a spray technique with an airbrush (c).

On the other hand, the SEM investigation was carried out in the backscattering mode, with a low vacuum condition of 100 Pa. Using the SEM the meta-shell prototype was examined both before and after the compression tests (see section 2.3), to investigate the surface morphology and the printing quality. Specifically, before the compression tests, the SEM investigations were aimed at measuring the thickness of the vertical ligaments at 20 different points of the structure. Similarly, after compression testing, the SEM scan, which required the specimen to be cleaned in an ultrasonic bath with acetone, aimed to identify any eventual failure surfaces in the meta-shell.

2.3. Experimental analysis

2.3.1. Mechanical testing. To assess the *quasi-static* mechanical performance of the AM-ed meta-shell, a compression test (figure 2(a)) was performed using a *MTS 858 Bionix* test machine, equipped with a 25 kN load cell. The test procedure consisted of a preload of up to 180 N, followed by three subsequent compression steps at a rate of 1 mm min^{-1} , up to 1%, 2% and 3% of the initial height of the prototype, respectively. During the test, we registered the compression force and the corresponding stroke of the loading plate of the testing machine.

A pseudo-multi-view DIC system [45, 55] was set up to acquire the required set of stereo images needed to compute the full-field 3D displacement maps of the meta-shell on its entire 360° outer surface (see section 2.3.2.). Prior to testing, as the DIC algorithm requires material continuity within each pixel subset, a thin layer of a soft modeling clay was applied from the inside of the shell (figure 2(b)) to fill the voids of the meta-structure. Then, the outer surface of the prototype was

airbrushed to create a stochastic distribution of black speckles on a white background (figure 2(c)), as required for the DIC measurement.

2.3.2. 3D DIC measurements. To perform full-field DIC shape and deformation measurements over the entire outer surface of the prototype, a pseudo-multicamera system was set up [55]. Instead of a polar array of cameras evenly distributed to cover the full 360° geometry, two stereo cameras (Sony IMX179 3263 \times 2448 pixels sensor, 5–50 mm lens) were mounted on a rotating ring coaxial with the load system and securely attached to the load machine frame base (figure 3). At each stage of the quasi-static compression test, the stereo cameras were successively positioned at 8 predetermined angular positions so as to span the entire surface of the meta-structure with a sufficiently large area of overlap between adjacent fields of view (FOV). Given the small axial size of the sample, it was possible to mount the cameras with a vertical parallax thus maximizing the extent of the common FOV. This resulted in a reduced number of angular positions required to cover the full 360° while still maintaining image sharpness in the peripheral areas of the prototype [45]. An LED ring light attached to the camera frame allowed uniform illumination of the region of interest (ROI) of the sample captured at each angular position.

Once the optimal lens parameters were set, the cameras were fixed symmetrically to the middle plane of the sample at a stereo angle of approximately 20° . A 3D calibration target was used to calculate the intrinsic (with radial distortion) and extrinsic parameters of the cameras [56]. Once the cameras were calibrated, a pair of images was captured at each of the eight predetermined angular positions for each load step of interest. The stereo images



Figure 3. The pseudo-multicamera DIC system setup to perform shape and deformation measurements over the entire 360° surface of the meta-structure. Two video cameras in stereo configuration are mounted on a rotating ring that is coaxial with the load application system and rigidly fixed to the machine base. The camera pair is successively positioned at eight predetermined angles around the 360° to capture the stereo images required for the DIC measurement.

were then processed using an in-house developed DIC software coded in *Matlab*. The description of the algorithms implemented in the DIC code used for the measurement is detailed in [57], together with a report of its metrological performance.

The DIC software used in this work allows for large deformation analysis without the need for a serial approach [58]. It is therefore possible to analyze the image pair of any deformed configuration by directly correlating it with its counterpart in the undeformed configuration. For each deformed state, an image pair was acquired simultaneously by the two stereo cameras at each angular position. The time required to acquire the eight stereo-images was approximately 1 min for each loading step.

The image processing procedure starts with the definition of a mask to delineate the ROI and the initialization of the image registration using the Scale Invariant Feature Transform algorithm [59]. The seed points obtained from this preliminary step can be used as initial guess for the subsequent DIC analysis. A subset-based DIC algorithm is then used to match a dense regular grid of points in each stereo image pair and then to track them through the temporal sequence of deformed images. It is hence possible to reconstruct the 3D point cloud for each part of the shell as it was captured at the eight angular positions. Finally, the 3D data are merged into a common coordinate frame with an optimization routine that finds the optimal rigid transformation that overlaps adjacent patches with the minimum error.

From the 3D coordinates of the undeformed and deformed configurations, displacement and strain maps can be calculated at more than 139 000 points over the entire outer surface of the meta-structure [57].

2.4. Numerical analysis

In order to develop a model capable of accurately predicting the response of the structure which can also be used for improving the design, a 3D FE model of the AM-ed meta-shell was implemented using the commercial *Abaqus* software. On the basis of the information obtained from the optical measurement described in section 2.2, the FE model accurately reproduced the meta-structure and, in particular, the accurate height of each vertical ligament at the top and bottom faces of the structure.

Figure 4(a) shows the second-order tetrahedral element mesh applied to the structure. A preliminary mesh sensitivity analysis was performed to determine the appropriate number of elements in the chiral ligaments of the meta-shell. In particular, the mesh density was increased until to the peak of the von Mises stress in the chiral connections converged satisfactory and the results not overly demanding of computational resources. Thus, the average side length of the mesh was set equal to 0.19 mm, for a total of approximately ten million degrees of freedom (DOF). The FE model describes the plates of the testing machine as rigid analytical (meshless) surfaces (figure 4(a)): thus, the model implements a general hard contact with a small sliding formulation and a friction coefficient equal to 0.4 between the vertical ligaments of the meta-shell and the surfaces representing the plates [60]. The numerical model implemented the material behavior of the titanium alloy using an isotropic elasto-plastic constitutive law with hardening, where the material data were retrieved from uniaxial tensile tests on dog-bone specimens according to the standard [61], which were provided by the manufacturer (*Zare Prototipi*, Reggio Emilia, Italy). Specifically, the Young's

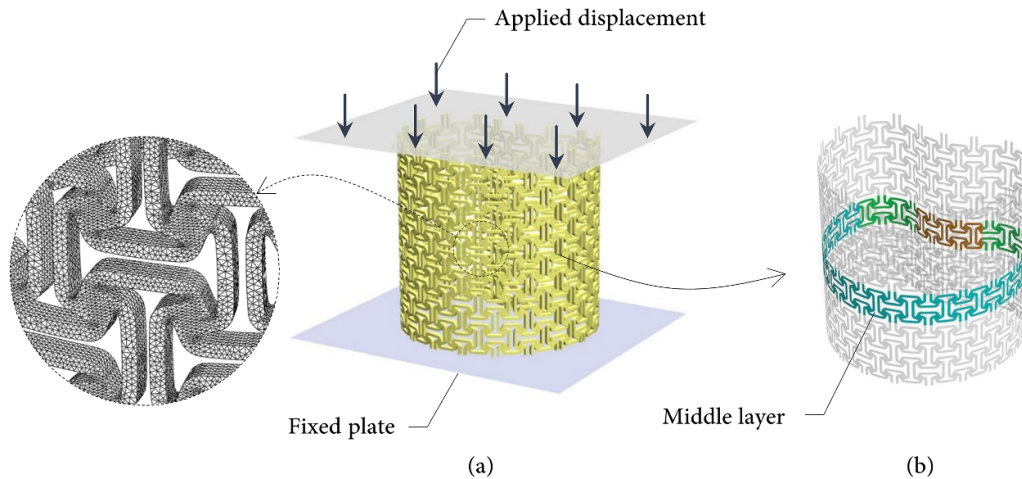


Figure 4. Schematic of the simulated meta-shell design implement in the finite element (FE) model with detail on the FE mesh for the chiral cells (a). Middle layer of the structure used for the calculation of Poisson's ratio of the meta-shell (b).

modulus, E_m , was set to 110 GPa, the PR, ν_m , was set to 0.34, the yield stress of the alloy material, $\sigma_{y,m}$, was set to 1.1 GPa, whilst the ultimate tensile strength of the parent material, $\sigma_{uts,m}$, was set equal to 1.2 GPa. It is worth noting that, the stress–strain data of the parent material are close to those of average post-processed AM TI-6Al–4V ELI retrieved from the literature [62].

In accordance with the test, the FE model applied a fixed constraint to the bottom plate, while three successive steps of downward compressive displacement were applied to the top plate, while constraining all remaining rotation and translation DOFs, figure 4(a).

The FE model allowed the PR to be evaluated along the central layer of elemental cells of the structure, using the procedure described in section 3.3. Therefore, in order to accurately evaluate the strain of the meta-shell, a more refined numerical model was implemented, using a finer mesh only in the central layer of the structure (figure 4(b), side element length equal to 0.1 mm).

3. Results

3.1. Morphology of the meta-shell

The SEM images in figure 5 show some details of the surface microstructure of the prototype: in particular, figures 5(a) and (b), refer to the prototype before the experimental tests, showing a detail of a vertical ligament, and the view of a unit cell, respectively. In contrast, figures 5(c) and (d) show the prototype after the compression tests: figure 5(c) focuses on a chiral unit, while figure 5(d) shows a close-up view of the connection between the chiral ligament and the solid central unit.

3.2. Full-field displacement and strain distributions

Figure 6 shows the full-field maps of the meta-shell obtained from the DIC measurement and the FE analysis. In order to obtain a consistent quantitative comparison between the experimental and the numerical data, the node coordinates of the

outer surface of the meta-shell were extracted from the FE model and processed with the same codes used for the DIC points grid.

Figures 6(a) and (b) show the distribution of the displacement components along the axial and radial directions, respectively. Figure 6(c) and d show an illustrative example of the strain maps obtained with the two approaches. In particular, the von Mises strain maps have been calculated for a global axial strain of the structure $\varepsilon_a = 2\%$. It should be noted that the experimental strain map includes the portions of the sample filled with clay whose strain level is one order of magnitude higher than the strain of the meta-shell. A closer view of the strain distribution of the unit cell (at the middle layer of the body segment) is shown in figure 6(d).

3.3. Quasi-static mechanical performance

The high spatial resolution of the measurement points for both the DIC and the FE model allowed a full-field estimate of the PR of the metamaterial. However, due to the sensitivity of the strain to noise, the experimental and the numerical displacement maps, plotted in cylindrical coordinates in figure 6, were interpolated with high-stiffness *NURBS* in a CAD environment. This acted as a low-pass filter, eliminating the local fluctuations in the displacement field due to the non-continuous nature of the structure.

Both the DIC data points and the FE model nodes were then resampled with a coarser grid of points regularly spaced along the axial and circumferential directions, for which the corresponding shape and displacement values were interpolated from the original data. Figure 7 illustrates this procedure: the figures in the first row show the original high-density grid in cylindrical coordinates (figure 7(b)) and the corresponding displacement map (figure 7(c)); the figures in the second row show the resulting sampled grid (figure 7(e)) after the filtering procedure of the displacement maps (figure 7(d)). In the left column, figure 7 shows the original (figure 7(a)) and resampled (figure 7(f)) geometries of the meta-shell.

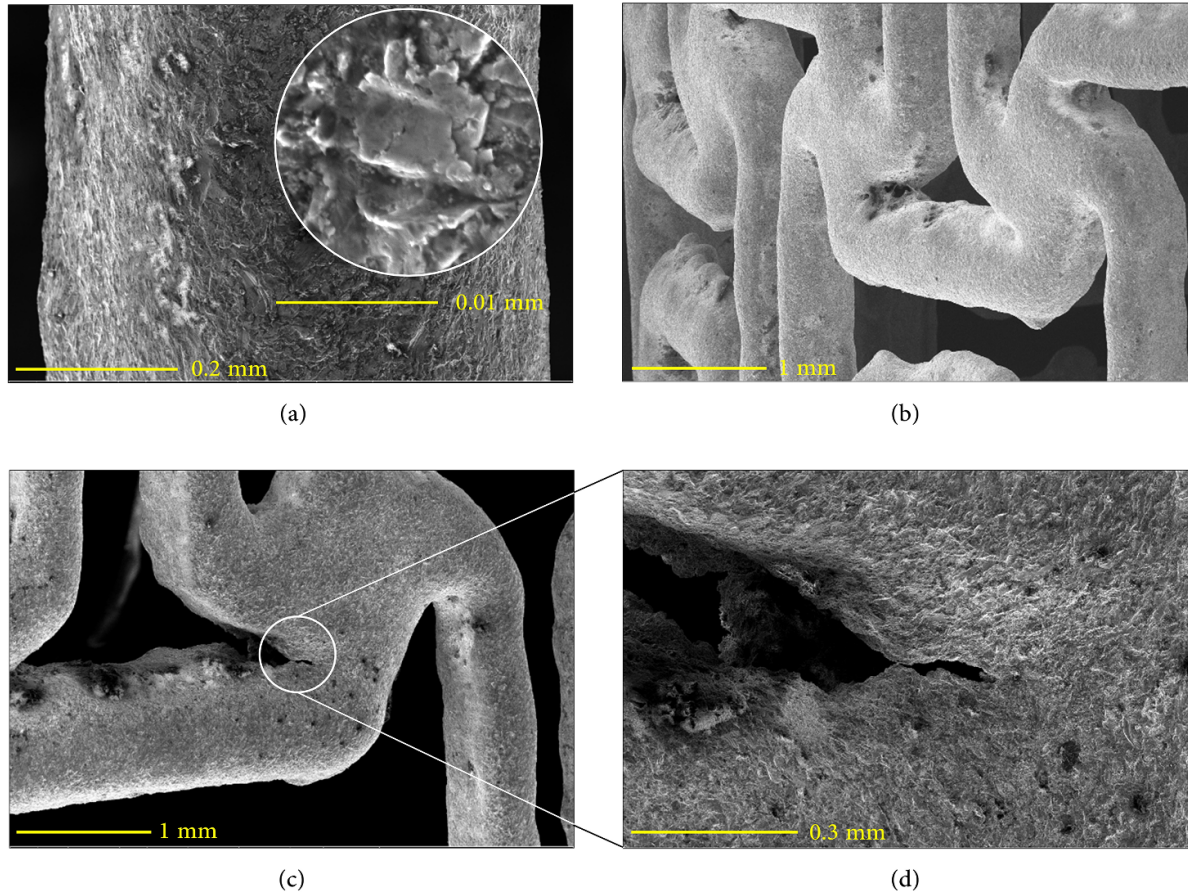


Figure 5. SEM images of the surface microstructure of the AM-ed meta-shell before the mechanical testing: vertical ligament of the structure with a detail on powder particles (a) and chiral units of the prototype (b). In (c) and (d) the Figures present a close-up view of the connection between the chiral strut and the central unit following the experiments, respectively.

This procedure allowed easy calculation of the PR of the meta-shell from the extracted data points: first, the elongation Δh and Δc of contiguous segments were calculated in the longitudinal and the circumferential directions, respectively (see inset in figure 7(f)). Then, the axial strain $\varepsilon_{a,i}$, and circumferential strain, $\varepsilon_{c,i}$, were calculated as the ratio of elongations to the undeformed lengths for each side of the rectangular grid in figure 7(f). Finally, a rough estimate of the local PRs of the meta-shell was calculated using the following expression:

$$\nu_i = -\frac{\varepsilon_{i,c}}{\varepsilon_{i,a}}. \quad (1)$$

Figure 8 shows the Poisson's ratio (PRs) calculated from the experimental and numerical data for four circular sectors at the mid-section of the structure, for a global strain of the structure $\varepsilon_a = 2\%$.

Figure 9(a) compares the experimental and numerical load-displacement curves of the investigated meta-shell. The plot shows two curves for the FE model: the black dashed line corresponds to a Young's modulus E_m of 110 GPa, while the orange dashed curve to a reduced Young's modulus E_r of 60 GPa, where the latter takes into account the artefacts and the irregularities of AM process that are not implemented in the FE model (see [27].): this value can be easily found by a cross-multiply.

Figure 9(b) shows the equivalent von Mises stress acting on the chiral cells along the middle layer of the metamaterial, for a global axial strain of the structure equal to 3%: these results were obtained from a dedicated FE model (see section 2.4) with a finer mesh on the middle layer of the structure, with an average element side equal to 0.1 mm. This mesh corresponds to approximately 12 layers of elements through the thickness of the ligaments and ensures stress convergence.

4. Discussion

4.1. Morphological characteristics

The SEM images in figure 5 provide some interesting insights useful for understanding the mechanical behavior of the AM-ed meta-shell. In particular, the SEM images of the prototype taken prior to testing (figure 5(a)) reveal the good surface morphology of the vertical ligaments of the chiral cells. Accordingly, the average cross section of the vertical struts measured by SEM images is almost equal to 590 μm , corresponding to a relative difference of less than 10% compared to the nominal ligament size in the CAD model.

Conversely, as shown in figure 5(b), the horizontal ligaments of the AM-ed meta-shell consistently exhibited significant geometric irregularities and microstructural defects,

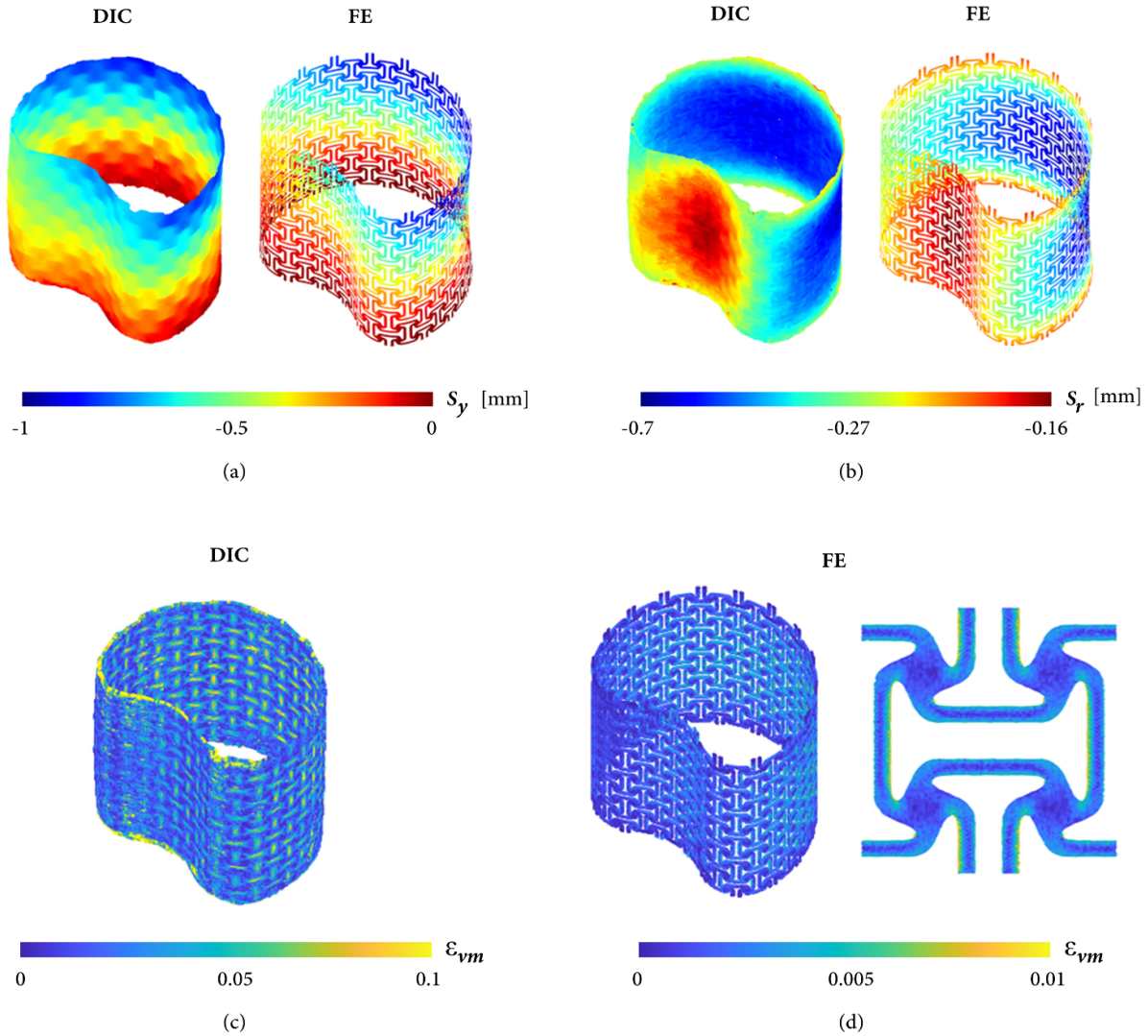


Figure 6. Experimental (DIC) and numerical (FE) distribution of the displacement components of the meta-shell along the axial (a) and radial (b) direction, calculated for a global axial strain of the structure $\varepsilon_a = 2\%$. Equivalent von Mises strain map of the meta-shell: Experimental results (c) and FE results (d), where the latter shows a detail on a chiral unit in the middle layer of the structure.

leading to undesirable porosities, especially along the upper side of these struts. These irregularities are mainly attributed to the orthogonal orientation of such ligaments with respect to the print orientation, and to the weight effect of the molten metal [63], which causes more irregular and larger struts. In particular, figure 5(b) highlights a more rounded cross-section for both the vertical and the horizontal struts of the chiral cells compared to those in the CAD model. A geometrical inaccuracy also appears in the connection region between the horizontal chiral ligaments and the rotating units: sharp fillet corners were obtained instead of variable-spline curvature joints, leading to an increase in the stress concentrations, and lower strength of the meta-structure [26, 64]. Some of these deviations in the geometric accuracy of the struts from the CAD model can also be attributed to the sandblasting process required to remove the support pillars between the horizontal ligaments.

On the other hand, the SEM inspections of the meta-shell after the mechanical test (figures 5(c) and (d)), revealed the

presence of micro-cracks in the junction region of the chiral cells, which in most cases originated close to surface inclusions (weak spots) [65]. This result confirms that crack initiation generally occurs at the interface between the strut and the cell [64, 66]. It is worth noting that the AM-ed meta-shell did not show any macroscale failure after experimental testing.

4.2. Experimental and numerical full-field maps

From the observation of the full-field displacement maps of the meta-shell reported in figures 6(a) and (b), it is possible to notice the non-uniform displacement magnitude along the entire external surface of the meta-structure. In particular, the results of figure 6(a) highlight that the axial displacement s_y of the prototype is not uniform in the circumferential direction, with a maximum compression of the structure in the *body* and in the left-side *peduncle* circular sectors. Accordingly, the value of s_y is different from zero in some regions of the lower sector of the vertebral meta-shell. This non-uniform

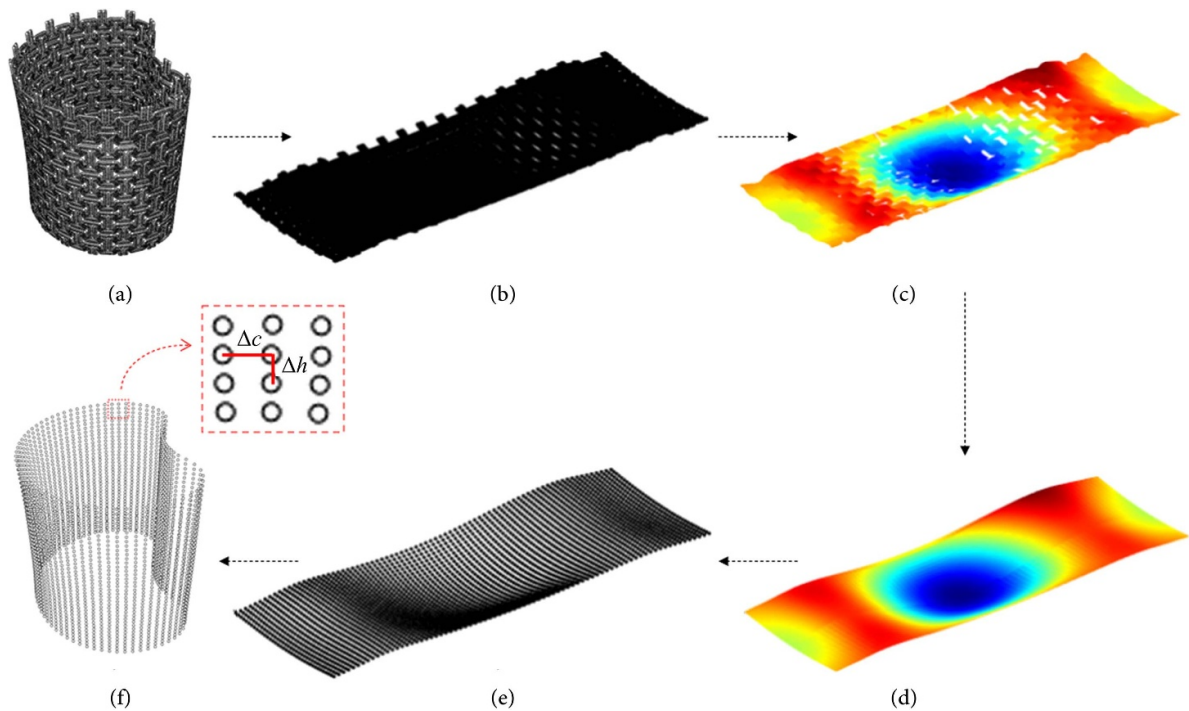


Figure 7. Data processing for the PR calculation from experimental and numerical data. The original point grid (a), original point cloud in cylindrical coordinates (b), radial displacement map (c), smooth radial displacement map (d), resampled data in cylindrical coordinates (e) and final point cloud for PR calculation (f).

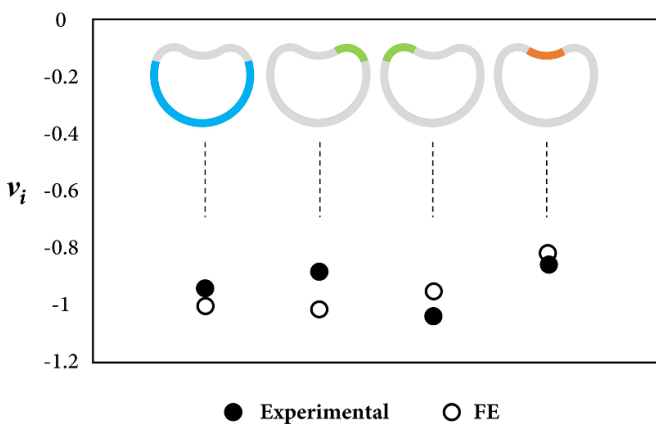


Figure 8. Comparison between the experimental and numerical Poisson's ratio of the meta-shell for the four circular sectors at the mid-section of the structure (see section 2.1).

displacement is caused by the fact that the upper and lower faces of the prototype were not perfectly parallel, due to the difference in the length of the vertical ligaments. Moreover, as shown in figure 6(a), the experimental and the numerical maps are in very good agreement, with a relative difference below 5% in the peak of compressive displacement.

A similar trend can be seen from the plots in figure 6(b), which show that the radial displacement distribution in the structure, denoted as s_r , reveals the heterogeneous stiffness of the meta-shell. In fact, the difference in the radial displacement distribution shown in figure 6(b), is strictly correlated to the different curvatures of the cylindrical sectors composing the

meta-shell. In particular, figure 6(b) underlines that the *body* sector has a lower radial stiffness with respect to both *canal* and *peduncle* sectors, and therefore shows a more pronounced radial contraction. On the other hand, due to the effect of the friction between the vertical ligaments on the upper and lower faces of the meta-shell with the load plates, the magnitude of the radial displacement in these regions is close to zero, with a good quantitative agreement between the experimental and FE results (see figure 6(b)).

The results in figures 6(c) and (d) indicate a clear similarity in the equivalent von Mises strain distribution, ε_{vm} , along the chiral cells of the structure between the DIC measurements and the numerical model. It is important to emphasize that experimental Green's strain maps shown in figure 6(c) describe the homogenized strain of the entire surface including the meta-shell struts and the clay used to fill the voids. In fact, each area of the surface sampled by the 21×21 pixels subset used for the DIC analysis is considered as a continuum by the algorithm, with a consequent low-filtering of the real displacement distribution. Nevertheless, due to the high spatial resolution of the camera sensor, DIC was able to reveal the different mechanical response of the meta-shell struts (distinguishable as areas with the lower strain levels in figure 6(c)) and the highly deformable filler. As a result, there is a good agreement between the strain levels of the ligaments predicted by FE analysis (figure 6(d)) and their experimental counterparts (figure 6(c)). Similar to the FE analysis, an accurate evaluation of the strain distribution at the level of individual struts (see magnified view of the strain on a single cell with the finest mesh in figure 6(d)) would require working with a very high

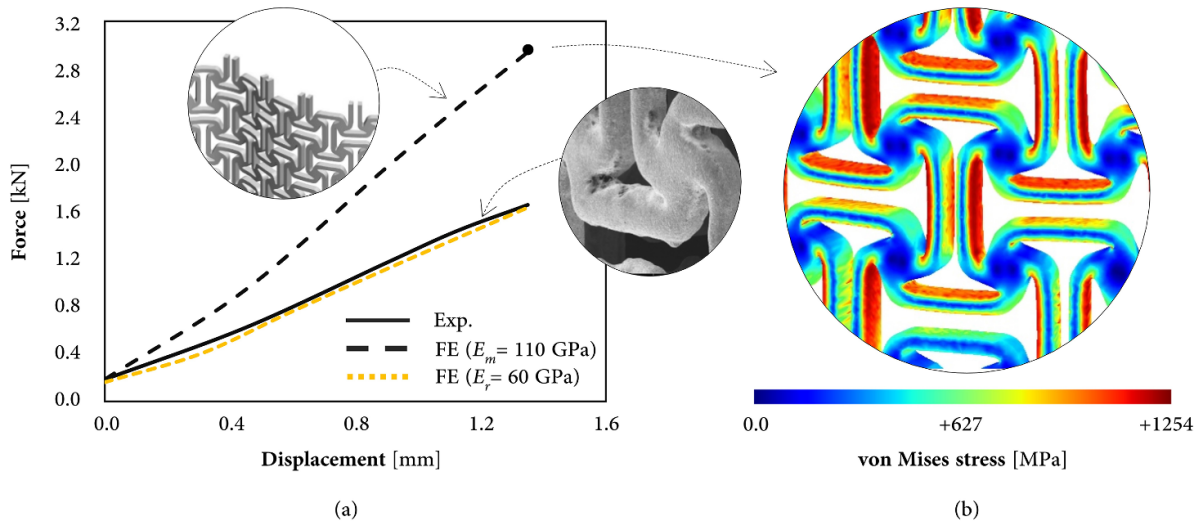


Figure 9. Comparison between the experimental and numerical force-displacement curves of the meta-shell with close-up view of ligament geometries (a); von Mises stress contour on the middle layer of the meta-shell (b), evaluated at a global strain of the structure $\varepsilon_a = 3\%$.

magnification factor. In this way, the DIC subset can be set smaller than the cross-sectional size of the chiral ligament and the displacement gradients can be correctly sampled at the cost of reducing the FOV [67].

Finally, the von Mises maps in figure 9(b) show that the chiral ligaments of the structure are clearly subjected to bending deformation. The discrepancy between the (rounded) real cross-section of the strut and its rectangular cross-section in the FE model will therefore result in a lower bending stiffness of the tested meta-structure.

4.3. Static mechanical properties

The plot in figure 8 shows that all the four circular sectors at the mid-section of the structure exhibit an NPR. In particular, as plotted in figure 8, in the *body* and *peduncle* regions, the PR reaches a value ranging between -0.9 to -1.04 , further highlighting the good quantitative agreement between the experimental data and the numerical model. As expected, the *canal* sector exhibits a higher PR compared to the other sectors, with an experimental value close to -0.86 . This variation in PR is due to the greater stiffness of the *canal* sector compared to the *body*, as a result of its specific geometric curvature. Overall, the results in figure 8 show how the peculiar morphology of the designed meta-shell is capable of exhibiting a high auxetic potential, thus preserving the typical NPR behavior observed in the 2D chiral geometry of figure 1(a). Animations showing the auxetic behavior of the meta-shell are presented in the supplementary material.

From the force-displacement curves in figure 9(a) it can be seen that, with the exception of the initial response, the metamaterial exhibits an almost linear behavior for a global deformation of the structure up to 3% of its original height. Hence, from the results in figure 9(a), we calculated the experimental elastic modulus using the overall engineering stress and strain of the meta-shell, according to [27]. The experimental Young's modulus of the meta-structure was found equal to

427 MPa. In particular, it is interesting to note that the experimentally obtained stiffness value of the meta-structure largely overlaps with the typical range of the *apparent* elastic modulus of human vertebral cortical-cancellous bones, with value ranging from 87 up to 791 MPa [68]. It is also pointed out that, to the authors' knowledge, the *apparent* elastic properties of human vertebral bones, such as Young's modulus and yield strength, have been investigated only on the level of the entire bones [68, 69] and particularly, on the level of the cancellous tissue, whose elastic moduli vary between 10 to 7976 MPa [70, 10, 14]. Furthermore, it is important to notice that, as reported in some works from the literature [71–73], both cortical and spongy vertebral tissues have similar contribution in the load bearing capacity of the vertebral body: this fact emphasizes the need of a cortical shell that replicates the elastic modulus of spongiosa. In addition, there is no scientific reason for the yield strength to be comparable to that of human bones [26]: thereby, an ideal meta-biomaterials should have the highest possible yield strength while maintaining the same elastic modulus of the native bony tissue [29]. However, the experimental curve in figure 9(a) shows a significantly lower stiffness of the AM-ed vertebral meta-shell compared to the numerical model (the dashed black curve in the figure 9(a)), where the latter assumed an elastic modulus of the base material, E_m , equal to 110 GPa. The discrepancy in these results can be attributed to two main issues. First, the significant difference between the nominal and manufactured geometry in terms of the shape of the chiral ligaments and the connections between ligaments and rotating units (details in figure 9(a)). Second, the presence of defects and porosities associated with the manufacturing process (see details in figure 9(a)), which have been discussed previously. Both issues (geometry and microstructure) can be accounted for by a significantly lower Young's modulus of the meta-shell in the computational model [74]. In this regard, we note that the dashed orange curve in figure 9(a), corresponding to a Young's modulus of 60 GPa, namely E_r , is in a very good agreement with its experimental counterpart. This points

to the need for accurate predictive numerical models to incorporate the actual geometry of the meta-shell, possibly including the typical imperfections caused by the AM process, which can be obtained, for example, from micro-computed tomography images of the prototype [75]. Furthermore, as shown in figure 9(b), the numerical prediction of the maximum von Mises stress, for a $\varepsilon_a = 3\%$, indicates that the stress raisers are concentrated along the chiral ligaments of the meta-structure, particularly along the vertical struts, which experienced an additional compressive loading. This result also confirms that the proposed meta-structure is capable of withstanding very high compressive loads, compatible with those acting along the spine [76], without any significant plastic deformation in the structure.

4.4. Main advantages and limitations

Currently, in vertebral surgeries, AM-ed VBRs represent a useful solution for the treatment of metastatic diseases. These type of prostheses are designed on the basis of preoperative imaging studies: they are uniquely ‘custom’ and produced for use in a specific individual, thus their structural properties are quite diverse between the different constructs [77]. Typically, conventional AM-ed VBR consist of a small hollow cylindrical or oval-shaped static device composed by a lattice-like structure and an outer thin shell [3]. The main drawback of AM-ed design found in the literature are the high stiffness of the internal porous lattice and the rigidity of the external shell, thus leading to increase bony reabsorption (i.e. a reduction in bone density) due to the stress-shielding effects, causing unstable fractures of the surrounding bone tissues [78]. An additional limitation is associated to the low bone stimulation and osseointegration rate of these devices, which reduce the bone migration inside the implant. Thus, only recently the advantages in the use of a porous cortical shell in artificial vertebral implants were investigated [79, 80]. Hence, there is a lack of data in literature on the mechanical properties and the long-term clinical outcomes of AM-ed spinal implants [81].

To prevent these potential adverse effects, this work can be regarded as the first attempt to design a novel deformable auxetic meta-shell showing a lower stiffness and higher elastic strain limit than the ordinary static AM-ed vertebral cages. Interestingly, the bone-stiffness matching solution proposed covers the spectrum of the elastic moduli of the healthy vertebral tissues, and particularly, shows the same order of magnitude in the Young’s modulus to that of cancellous counterpart: this could limit the bone resorption in the bone-implant interfaces. Among other potential advantages, this design prevents any contact with the surrounding spinal cord, meaning that, thanks to their auxetic ability it contracts transversally to the direction that experiences longitudinally compressive stress. Hence, an additional beneficial feature of the use of this design, is the high porosity of the meta-shell, aiming to promote the flow of nutrients and the growth of bony tissues inside the structure [82].

However, the main limitations of the use of this novel meta-shell in real life applications regard: (i) the connection of the meta-structure with the posterior screw-rod instrumentation used to stabilize the spine and (ii) the manufacturability constraints associated to the 3D printing process. Additionally, a better understating of the mechanical behavior of this meta-structure under complex multi-axial mechanical loads is required.

Finally, although the efficiency, the 3D motion and the clinical application of this meta-structure is yet to prove, we showed how to develop a novel complex multiple curved chiral auxetic meta-structure and hope that this work can act as a blueprint for the development of promising 3D-printed vertebral meta-implants with the required functionalities, such as a bone stiffness matching property.

5. Conclusions

This work reports on a joint experimental and numerical investigation of a newly designed biomimetic auxetic vertebral meta-shell that exhibits lower stiffness and higher elastic strain limit than conventional AM-ed vertebral cages. This can result in a significant reduction in stress shielding phenomena while promoting bone ingrowth within the meta-structure. The proposed meta-shell design can be used to create custom-made, functionalized vertebral meta-implants, i.e. orthopedic devices designed using meta-biomaterials, that benefit from the unusual mechanical properties offered by auxetic metamaterials. Future studies will consider the integration of an NPR bone-mimicking scaffold inside this meta-shell, able to preserve the auxetic effect of the implant while aiming to minimize the weight and the stiffness of the whole prosthesis.

Data availability statement

The data cannot be made publicly available upon publication because they are not available in a format that is sufficiently accessible or reusable by other researchers. The data that support the findings of this study are available upon reasonable request from the authors.

Conflict of interest

The author(s) declared no potential conflicts of interest with respect to the research, authorship, and/or publication of this article.

Funding

The work is partially funded by the ESF REACT-EU: Programma Operativo Nazionale (PON) ‘Ricerca e Innovazione’ 2014–2020, CCI2014IT16M20P005, Progetti DM 1062 del 10/08/2021.

ORCID iDs

A Sorrentino  <https://orcid.org/0000-0002-7145-5219>
 D Castagnetti  <https://orcid.org/0000-0003-3300-5716>

References

- [1] Sundaresan N, Rosen G and Boriani S 2009 Primary malignant tumors of the spine *Orthop. Clin. N. Am.* **40** 21–36
- [2] Kurisunkal V, Gulia A and Gupta S 2020 Principles of management of spine metastasis *Indian J. Orthop.* **54** 181–93
- [3] Boriani S, Gasbarrini A, Bandiera S, Ghermandi R and Lador R 2017 En bloc resections in the spine: the experience of 220 patients during 25 years *World Neurosurg.* **98** 217–29
- [4] Lewandrowski K-U, Hecht A C, DeLaney T F, Chapman P A, Hornicek F J and Pedlow F X 2004 Anterior spinal arthrodesis with structural cortical allografts and instrumentation for spine tumor surgery *Spine* **29** 1150–8
- [5] Boriani S, Biagini R, Bandiera S, Gasbarrini A and De Iure F 2002 Reconstruction of the anterior column of the thoracic and lumbar spine with a carbon fiber stackable cage system *Orthopedics* **25** 37–42
- [6] Dvorak M F, Kwon B K, Fisher C G, Eiserloh H L, Boyd M and Wing P C 2003 Effectiveness of titanium mesh cylindrical cages in anterior column reconstruction after thoracic and lumbar vertebral body resection *Spine* **28** 902–8
- [7] Viswanathan A, Abd-El-Barr M M, Doppenberg E, Suki D, Gokaslan Z, Mendel E, Rao G and Rhines L D 2012 Initial experience with the use of an expandable titanium cage as a vertebral body replacement in patients with tumors of the spinal column: a report of 95 patients *Eur. Spine J.* **21** 84–92
- [8] Girolami M, Boriani S, Bandiera S, Barbanti-Bródano G, Ghermandi R, Terzi S, Tedesco G, Evangelisti G, Pipola V and Gasbarrini A 2018 Biomimetic 3D-printed custom-made prosthesis for anterior column reconstruction in the thoracolumbar spine: a tailored option following en bloc resection for spinal tumors: preliminary results on a case-series of 13 patients *Eur. Spine J.* **27** 3073–83
- [9] Girolami M, Sartori M and Bandiera S 2022 *3D Vertebral Prosthesis BT—3D Printing in Bone Surgery* ed C Zoccali, P Ruggieri and F Benazzo (Springer) pp 97–104
- [10] Rho J Y, Kuhn-Spearing L and Zioupos P 1998 Mechanical properties and the hierarchical structure of bone *Med. Eng. Phys.* **20** 92–102
- [11] Costanzo R et al 2022 The role of 3D-printed custom-made vertebral body implants in the treatment of spinal tumors: a systematic review *Life* **12** 1–14
- [12] Angelini A, Trovarelli G, Berizzi A, Pala E, Breda A and Ruggieri P 2019 Three-dimension-printed custom-made prosthetic reconstructions: from revision surgery to oncologic reconstructions *Int. Orthop.* **43** 123–32
- [13] Warburton A, Girdler S J, Mikhail C M, Ahn A and Cho S K 2020 Biomaterials in spinal implants: a review *Neurospine* **17** 101–10
- [14] Barba D, Alabort E and Reed R C 2019 Synthetic bone: design by additive manufacturing *Acta Biomater.* **97** 637–56
- [15] Pawelec K M and Planell J A 2018 *Bone Repair Biomaterials: Regeneration and Clinical Applications* (Woodhead Publishing)
- [16] Bobbert F S L and Zadpoor A A 2017 Effects of bone substitute architecture and surface properties on cell response, angiogenesis, and structure of new bone *J. Mater. Chem. B* **5** 6175–92
- [17] Ngo T D, Kashani A and Imbalzano G, Nguyen K T and Hui D 2018 Additive manufacturing (3D printing): a review of materials, methods, applications and challenges *Composites B* **143** 172–96
- [18] Tappa K and Jammalamadaka U 2018 Novel biomaterials used in medical 3D printing techniques *J. Funct. Biomater.* **9** 17
- [19] Yáñez A, Cuadrado A, Martel O, Afonso H and Monopoli D 2018 Gyroid porous titanium structures: a versatile solution to be used as scaffolds in bone defect reconstruction *Mater. Des.* **140** 21–29
- [20] Kelly C N, Miller A T, Hollister S J, Guldberg R E and Gall K 2018 Design and structure–function characterization of 3D printed synthetic porous biomaterials for tissue engineering *Adv. Healthcare Mater.* **7** 1–16
- [21] Mirzaali M J and Zadpoor A A 2024 Orthopedic meta-implants *APL Bioeng.* **8** 010901
- [22] Zadpoor A A 2017 Mechanics of additively manufactured biomaterials *J. Mech. Behav. Biomed. Mater.* **70** 1–6
- [23] Mohammad-shahi M H and Nikolaou V S 2013 The effect of angular mismatch between vertebral endplate and vertebral body replacement endplate on implant subsidence *J. Spinal Disord. & Tech.* **26** 268–73
- [24] Uchida K, Kobayashi S, Matsuzaki M, Nakajima H, Shimada S, Yayama T, Sato R and Baba H 2006 Anterior versus posterior surgery for osteoporotic vertebral collapse with neurological deficit in the thoracolumbar spine *Eur. Spine J.* **15** 1759–67
- [25] Vyavahare S, Mahesh V, Mahesh V and Harursamphath D 2023 Additively manufactured meta-biomaterials: a state-of-the-art review *Compos. Struct.* **305** 116491
- [26] Zadpoor A A 2019 Mechanical performance of additively manufactured meta-biomaterials *Acta Biomater.* **85** 41–59
- [27] Kolken H M A, Lietaert K, van der Sloten T, Poursan B, Meynen A, Van Loock G, Weinans H, Scheyls L and Zadpoor A A 2020 Mechanical performance of auxetic meta-biomaterials *J. Mech. Behav. Biomed. Mater.* **104** 103658
- [28] Lvov V A, Senatov F S, Veveris A A, Skrybykina V A and Díaz Lantada A 2022 Auxetic metamaterials for biomedical devices: current situation, main challenges, and research trends *Materials* **15** 1–26
- [29] Chen D, Li D, Pan K, Gao S, Wang B, Sun M, Zhao C, Liu X and Li N 2022 Strength enhancement and modulus modulation in auxetic meta-biomaterials produced by selective laser melting *Acta Biomater.* **153** 596–613
- [30] Huang H, Wang L and Fan Y 2023 Metallic meta-biomaterials: a critical review of fatigue behaviors *J. Sci.* **8** 100585
- [31] Kolken H M A, Garcia A F, Du Plessis A, Rans C, Mirzaali M J and Zadpoor A A 2021 Fatigue performance of auxetic meta-biomaterials *Acta Biomater.* **126** 511–23
- [32] Alomarah A, Yuan Y and Ruan D 2023 A bio-inspired auxetic metamaterial with two plateau regimes: compressive properties and energy absorption *Thin-Walled Struct.* **192** 111175
- [33] Lakes R S 2017 Negative-poisson's-ratio materials: auxetic solids *Annu. Rev. Mater. Res.* **47** 63–81
- [34] Zhou X, Ren L, Song Z, Li G, Zhang J, Li B, Wu Q, Li W, Ren L and Liu Q 2023 Advances in 3D/4D printing of mechanical metamaterials: from manufacturing to applications *Composites B* **254** 110585
- [35] Ren X, Das R, Tran P, Ngo T D and Xie Y M 2018 Auxetic metamaterials and structures: a review *Smart Mater. Struct.* **27** 023001
- [36] van Manen T, Ganjian M, Modaresifar K, Fratila-Apachitei L E and Zadpoor A A 2023 Automated folding of origami lattices: from nanopatterned sheets to stiff meta-biomaterials *Small* **19** 2203603

- [37] Lee J W, Soman P, Park J H, Chen S and Cho D W 2016 A tubular biomaterial construct exhibiting a negative poisson's ratio *PLoS One* **11** 1–14
- [38] Solak K and Orhan S N 2024 Quasi-static crashworthiness behaviour of auxetic tubular structures based on rotating deformation mechanism *Smart Mater. Struct.* **33** 055016
- [39] Solak K and Orhan S N 2023 Performance evaluation of peanut-shaped tubular auxetics with enhanced stiffness: a finite element study *Modelling Simul. Mater. Sci. Eng.* **31** 015006
- [40] Kolken H M A, Janbaz S, Leeftang S M A, Lietaert K, Weinans H H and Zadpoor A A 2018 Rationally designed meta-implants: a combination of auxetic and conventional meta-biomaterials *Mater. Horiz.* **5** 28–35
- [41] Sorrentino A and Castagnetti D 2022 Negative Poisson's ratio lattice for designing vertebral biomaterials *Mech. Adv. Mater. Struct.* **29** 6626–33
- [42] Sorrentino A and Castagnetti D 2023 Novel polyhedral mechanical metamaterial exhibiting negative Poisson's ratio *Smart Mater. Struct.* **32** 035008
- [43] Sorrentino A and Castagnetti D 2024 Geometrically tunable architected materials designed from prismatic rotating units *Proc. Inst. Mech. Eng. L* **238** 1690–704
- [44] Sorrentino A and Castagnetti D 2024 Periodic tetrahedral auxetic metamaterial *Extrem. Mech. Lett.* **71** 102214
- [45] Pan B 2018 Digital image correlation for surface deformation measurement: historical developments, recent advances and future goals *Meas. Sci. Technol.* **29** 082001
- [46] Yarali E, Zadpoor A A, Staufer U, Accardo A and Mirzaali M J 2023 Auxeticity as a mechanobiological tool to create meta-biomaterials *ACS Appl. Bio Mater.* **6** 2562–75
- [47] Cowin S C 1986 Wolff's law of trabecular architecture at remodeling equilibrium *J. Biomech. Eng.* **108** 83–88
- [48] Sorrentino A, Castagnetti D, Mizzi L and Spaggiari A 2022 Bio-inspired auxetic mechanical metamaterials evolved from rotating squares unit *Mech. Mater.* **173** 104421
- [49] Sorrentino A, Castagnetti D, Mizzi L and Spaggiari A 2021 Rotating squares auxetic metamaterials with improved strain tolerance *Smart Mater. Struct.* **30** 035015
- [50] Sorrentino A, Castagnetti D, Spaggiari A and Dragoni E 2019 Shape optimization of the fillet under a bolt's head *J. Strain Anal. Eng. Des.* **54** 247–53
- [51] Mizzi L, Sorrentino A, Spaggiari A and Castagnetti D 2021 A comparison between rotating squares and anti-tetrachiral systems: influence of ligaments on the multi-axial mechanical response *Proc. Inst. Mech. Eng. C* **235** 7759–73
- [52] Zhou S H, McCarthy I D, McGregor A H, Coombs R R H and Hughes S P F 2000 Geometrical dimensions of the lumbar vertebrae—Analysis of data from digitised CT images *Eur. Spine J.* **9** 242–8
- [53] Suresh S, Sun C N, Tekumalla S, Rosa V, Ling Nai S M and Wong R C W 2021 Mechanical properties and in vitro cytocompatibility of dense and porous Ti–6Al–4V ELI manufactured by selective laser melting technology for biomedical applications *J. Mech. Behav. Biomed. Mater.* **123** 104712
- [54] Chen M, Huang J, Jiang W and Fu M 2022 Elastic properties of lightweight rotating square structures *Mater. Today Commun.* **33** 104256
- [55] Genovese K, Cortese L, Rossi M and Amodio D 2016 A 360-deg digital image correlation system for materials testing *Opt. Lasers Eng.* **82** 127–34
- [56] Tsai R Y 1987 A versatile camera calibration technique for high-accuracy 3D machine vision metrology using off-the-shelf TV cameras and lenses *IEEE J. Robot. Autom.* **3** 323–44
- [57] Genovese K 2019 An omnidirectional DIC system for dynamic strain measurements on soft biological parts to An omnidirectional DIC system for dynamic strain measurement on soft biological tissues and organs *Opt. Lasers Eng.* **116** 6–18
- [58] Bing P, D W and Xia Y 2012 Incremental calculation for large deformation measurement using reliability-guided digital image correlation *Opt. Lasers Eng.* **50** 586–92
- [59] Lowe D G 2004 Distinctive image features from scale-invariant keypoints *Int. J. Comput. Vis.* **60** 91–110
- [60] Seetoh I P, Liu X, Markandan K, Zhen L and Lai C Q 2021 Strength and energy absorption characteristics of Ti6Al4V auxetic 3D anti-tetrachiral metamaterials *Mech. Mater.* **156** 103811
- [61] American Society for Testing and Materials, ASTM D638-14 2016 Standard practice for preparation of metallographic specimens *ASTM Int.* **82** 1–15
- [62] Rafi H K, Karthik N V, Gong H, Starr T L and Stucker B E 2013 Microstructures and mechanical properties of Ti6Al4V parts fabricated by selective laser melting and electron beam melting *J. Mater. Eng. Perform.* **22** 3872–83
- [63] Murchio S, Du Plessis A, Luchin V, Maniglio D and Benedetti M 2024 Influence of mean stress and building orientation on the fatigue properties of sub-unital thin-strut miniaturized Ti6Al4V specimens additively manufactured via laser-powder bed fusion *Int. J. Fatigue* **180** 108102
- [64] du Plessis A, Razavi N, Benedetti M, Murchio S, Leary M, Watson M, Bhate D and Berto F 2022 Properties and applications of additively manufactured metallic cellular materials: a review *Prog. Mater. Sci.* **125** 100918
- [65] Zadpoor A A 2019 Additively manufactured porous metallic biomaterials *J. Mater. Chem. B* **7** 4088–117
- [66] Benedetti M, du Plessis A, Ritchie R O, Dallago M, Razavi N and Berto F 2021 Architected cellular materials: a review on their mechanical properties towards fatigue-tolerant design and fabrication *Mater. Sci. Eng. R* **144** 100606
- [67] Genovese K, Leeftang S and Zadpoor A A 2017 Microscopic full-field three-dimensional strain measurement during the mechanical testing of additively manufactured porous biomaterials *J. Mech. Behav. Biomed. Mater.* **69** 327–41
- [68] El Masri F, de Sapin Brosses E, Rhissassi K, Skalli W and Mitton D 2012 Apparent Young's modulus of vertebral cortico-cancellous bone specimens *Comput. Methods Biomech. Biomed. Eng.* **15** 23–28
- [69] Dall'Ara E, Karl C, Mazza G, Franzoso G, Vena P, Pretterklieber M, Pahr D and Zysset P 2013 Tissue properties of the human vertebral body sub-structures evaluated by means of microindentation *J. Mech. Behav. Biomed. Mater.* **25** 23–32
- [70] Öhman-Mägi C, Holub O, Wu D, Hall R M and Persson C 2021 Density and mechanical properties of vertebral trabecular bone—A review *JOR Spine* **4**
- [71] Eswaran S K, Gupta A, Adams M F and Keaveny T M 2006 Cortical and trabecular load sharing in the human vertebral body *J. Bone Miner. Res.* **21** 307–14
- [72] Andresen R, Werner H J and Schober H C 1998 Contribution of the cortical shell of vertebrae to mechanical behaviour of the lumbar vertebrae with implications for predicting fracture risk *Br. J. Radiol.* **71** 759–65
- [73] Eswaran S K, Bayraktar H H, Adams M F, Gupta A, Hoffmann P F, Lee D C, Papadopoulos P and Keaveny T M 2007 The micro-mechanics of cortical shell removal in the human vertebral body *Comput. Methods Appl. Mech. Eng.* **196** 3025–32
- [74] Dong G, Tang Y and Zhao Y F 2017 A survey of modeling of lattice structures fabricated by additive manufacturing *J. Mech. Des.* **139** 1–13
- [75] Kelly C N, Francovich J, Julmi S, Safranski D, Guldberg R E, Maier H J and Gall K 2019 Fatigue behavior of As-built selective laser melted titanium scaffolds with sheet-based gyroid microarchitecture for bone tissue engineering *Acta Biomater.* **94** 610–26

- [76] Han K S, Rohlmann A, Zander T and Taylor W R 2013 Lumbar spinal loads vary with body height and weight *Med. Eng. Phys.* **35** 969–77
- [77] Chin B Z, Ji T, Tang X, Yang R and Guo W 2019 Three-level lumbar en bloc spondylectomy with three-dimensional–printed vertebrae reconstruction for recurrent giant cell tumor *World Neurosurg.* **129** 531–537.e1
- [78] Brenke C, Fischer S, Carolus A, Schmieder K and Ening G 2016 Complications associated with cervical vertebral body replacement with expandable titanium cages *J. Clin. Neurosci.* **32** 35–40
- [79] Kang J, Dong E, Li X, Guo Z, Shi L, Li D and Wang L 2021 Topological design and biomechanical evaluation for 3D printed multi-segment artificial vertebral implants *Mater. Sci. Eng. C* **127** 112250
- [80] Liebsch C, Aleinikov V, Kerimbayev T, Akshulakov S, Kocak T, Vogt M, Jansen J U and Wilke H-J 2020 In vitro comparison of personalized 3D printed versus standard expandable titanium vertebral body replacement implants in the mid-thoracic spine using entire rib cage specimens *Clin. Biomech.* **78** 105070
- [81] Meena V K, Kumar P, Kalra P and Sinha R K 2021 Additive manufacturing for metallic spinal implants: a systematic review *Ann. 3D Print. Med.* **3** 100021
- [82] Lu T, Liu C, Yang B, Liu J, Zhang F, Wang D, Li H and He X 2017 Single-level anterior cervical corpectomy and fusion using a new 3D-printed anatomy-adaptive titanium mesh cage for treatment of cervical spondylotic myelopathy and ossification of the posterior longitudinal ligament: a retrospective case series study *Med. Sci. Monit.* **23** 3106–13